A flamelet-based model for supersonic combustion

By V. E. Terrapon, F. Ham, R. Pecnik AND H. Pitsch

1. Motivation and objective

The renewed interest in high-speed flight has recently demonstrated the need for the development of hypersonic air-breathing propulsion systems, i.e., in which the ambient air is used as oxidizer. These systems have long been recognized as the most well-suited for hypersonic propulsion. Although a traditional ramjet is most appropriate for supersonic speeds (Mach 3 to 5), hypersonic speeds (Mach 6 to15) can be reached only with the use of a scramjet, where combustion takes place at supersonic speeds. Because the internal flow in a scramjet is supersonic, the flow has a very short residence time during which air and fuel must mix on a molecular level, and chemical reactions have to be completed before leaving the engine. Moreover, the inlet flow is often accompanied by oblique shocks so that mixing, sustained combustion and flame anchoring become critical. Although some ground and flight experiments have successfully demonstrated the feasibility of supersonic combustion (e.g., Gardner *et al.* 2004; Smart, Hass & Paull 2006), experimental testing requires a large investment and presents numerous difficulties. Computational tools are thus a key element toward the development of an efficient, high-performance scramjet engine, and because mixing and heat release are at the heart of a scramjet operation, the implementation of an accurate combustion model for supersonic combustion is critical.

The vast majority of computational work in supersonic turbulent combustion has so far relied on simplified/reduced mechanisms and the explicit transport of the involved species (Bray 1996). Such approaches require the closure of the chemical source term in the species transport equation. This can be achieved, for example, with simpler but low-accuracy models such as Arrhenius law (Davidenko *et al.* 2003), which neglects closure, the Eddy Dissipation Concept model (Chakraborty, Paul & Mukunda 2000), or with closure based on assumed (Baurle & Girimaji 2003; Karl *et al.* 2008) or transported (Baurle, Hsu & Hassan 1995) probability distribution functions (PDF). Some authors have also used the Linear Eddy Mixing model (LEM) (Genin, Chernyavsky & Menon 2004). But due to the strong non-linearity of the source term and the wide range of time scales associated with the chemistry, those equations are very stiff and difficult to solve. Moreover, due to very short residence times in such high speed flows, flame stabilization mechanisms are governed by auto-ignition. It is critical to model accurately such ignition and extinction phenomena in order to predict the stability of scramjet combustion. Therefore, prediction of flame stabilization requires detailed chemical kinetics. While a model transporting all involved species can easily be extended to more detailed chemical mechanisms, it quickly becomes computationally intractable, especially when complex fuels must be considered.

An alternative approach is based on the flamelet concept (Peters 2000; Pitsch 2006), which assumes that the chemical time scales are shorter than the turbulent time scales so that the flame can be approximated as one-dimensional. The flamelet approach allows the computation of the chemistry to be performed independently of the combustor simulation and stored in tabulated form as function of a limited number of scalars. During the

actual scramjet simulation, the quantities of interest are read and interpolated, thus, dramatically decreasing the computational cost and allowing the use of complex chemical mechanisms. However, the implementation of the flamelet model is based on a low Mach number assumption, explaining the still very limited number of studies of high-speed flows using this approach (Berglund & Fureby 2007).

In the low Mach number flamelet implementation, the temperature and the species mass fraction are assumed to depend only on a transported scalar, traditionally the mixture fraction Z, and its dissipation rate. Chemical tables are then constructed assuming constant background pressure. This formulation can also be extended to better reproduce the unsteady character of combustion by replacing the scalar dissipation rate with a progress variable (Pierce & Moin 2004). However, the low Mach number assumptions do not hold anymore at supersonic speed and compressibility effects start to play an important role. Therefore, the flamelet implementation has been reformulated where temperature is no longer given by a chemistry table but computed from the total energy, thus, better accounting for compressibility effects (Birbaud & Pitsch 2008). Further, the model is extended for the auto-ignition regime with arguments similar to the model developed by Cook *et al.* (2007) for ignition in HCCI engines.

2. Combustion model for RANS

2.1. *Mathematical formulation*

In the following, the combustion model is based on the flamelet progress variable approach (FPVA) introduced by Pierce & Moin (2004). The steady flamelet model can be derived in a very similar way. The general form used for the set of equations is the conservative form. In this context, the balance equations for the conserved Favre averaged variables $\phi = \{\bar{\rho}, \bar{\rho}\widetilde{u}_i, \bar{\rho}\widetilde{Z}, \bar{\rho}\widetilde{Z''^2}, \bar{\rho}\widetilde{C}, \bar{\rho}\widetilde{E}\}^T$ read

$$\frac{\partial \bar{\rho}}{\partial t} + \frac{\partial \bar{\rho}\widetilde{u}_j}{\partial x_j} = 0, \tag{2.1}$$

$$\frac{\partial \bar{\rho}\widetilde{u}_i}{\partial t} + \frac{\partial \bar{\rho}\widetilde{u}_i\widetilde{u}_j}{\partial x_j} + \frac{\partial \bar{p}}{\partial x_i} = \frac{\partial}{\partial x_j}\left[(\mu+\mu_t)\left(\frac{\partial \widetilde{u}_i}{\partial x_j} + \frac{\partial \widetilde{u}_j}{\partial x_i} - \frac{2}{3}\delta_{ij}\frac{\partial \widetilde{u}_k}{\partial x_k}\right) - \frac{2}{3}\bar{\rho}k\delta_{ij}\right], \tag{2.2}$$

$$\frac{\partial \bar{\rho}\widetilde{Z}}{\partial t} + \frac{\partial \bar{\rho}\widetilde{u}_j\widetilde{Z}}{\partial x_j} = \frac{\partial}{\partial x_j}\left[\left(\bar{\rho}D + \frac{\mu_t}{Sc_t}\right)\frac{\partial \widetilde{Z}}{\partial x_j}\right], \tag{2.3}$$

$$\frac{\partial \bar{\rho}\widetilde{Z''^2}}{\partial t} + \frac{\partial \bar{\rho}\widetilde{u}_j\widetilde{Z''^2}}{\partial x_j} = \frac{\partial}{\partial x_j}\left[\left(\bar{\rho}D + \frac{\mu_t}{Sc_t}\right)\frac{\partial \widetilde{Z''^2}}{\partial x_j}\right] + 2\frac{\mu_t}{Sc_{t_2}}\frac{\partial \widetilde{Z}}{\partial x_j}\frac{\partial \widetilde{Z}}{\partial x_j} - C_\chi\bar{\rho}\frac{\epsilon}{k}\widetilde{Z''^2}, \tag{2.4}$$

$$\frac{\partial \bar{\rho}\widetilde{C}}{\partial t} + \frac{\partial \bar{\rho}\widetilde{u}_j\widetilde{C}}{\partial x_j} = \frac{\partial}{\partial x_j}\left[\left(\bar{\rho}D + \frac{\mu_t}{Sc_t}\right)\frac{\partial \widetilde{C}}{\partial x_j}\right] + \bar{\dot{\omega}}_C, \tag{2.5}$$

$$\begin{aligned}\frac{\partial \bar{\rho}\widetilde{E}}{\partial t} + \frac{\partial \bar{\rho}\widetilde{u}_j\widetilde{E}}{\partial x_j} =& \frac{\partial}{\partial x_j}\left[\left(\frac{\lambda}{c_p} + \frac{\mu_t}{Pr_t}\right)\frac{\partial \widetilde{h}}{\partial x_j} + \sum_{k=1}^{N}\left(\bar{\rho}D_k - \frac{\lambda}{c_{p_k}}\right)\widetilde{h}_k\frac{\partial \widetilde{Y}_k}{\partial x_j}\right] \\ &+ \frac{\partial}{\partial x_j}\left[\left(\mu + \frac{\mu_t}{\sigma_k}\right)\frac{\partial k}{\partial x_j} - \widetilde{u}_j\bar{p} + \widetilde{u}_i\left(\bar{\tau}_{ij} - \bar{\rho}\widetilde{u_i''u_j''}\right)\right],\end{aligned} \tag{2.6}$$

where $\bar{\rho}$ is the density, $\widetilde{u}_i$ the velocity, $\widetilde{Z}$ the mixture fraction, $\widetilde{Z''^2}$ the variance of the mixture fraction, $\widetilde{C}$ the progress variable, and $\widetilde{E}$ the total energy, including the chemical energy. The last term in the first line of the energy equation (2.6) vanishes under the unity Lewis number assumption $Le = 1$. The turbulent viscosity μ_t is computed with an adequate turbulence model, e.g., Spalart-Allmaras, k-ϵ or k-ω model, which is also used to compute the turbulent kinetic energy k and the turbulent dissipation rate ϵ. In the following, the Prandtl number is chosen to be $Pr = 0.5$, the Schmidt numbers $Sc_t = Sc_{t_2} = 0.5$, and the model constants $\sigma_k = 1$ and $C_\chi = 2$.

In the present formulation the total chemical energy is used, so that the chemical source term does not appear explicitly in the energy equation (2.6) (Poinsot & Veynante 2005). $\widetilde{E}$ is expressed by $\widetilde{E} = \widetilde{h} - \bar{p}/\bar{\rho} + 1/2\widetilde{u}_k^2 + k$, where $\bar{p}$ refers to the pressure and $\widetilde{h}$ to the chemical and sensible enthalpy of the N species mixture:

$$\widetilde{h} = \sum_{k=1}^{N} \widetilde{Y}_k h_k(\bar{T}), \tag{2.7}$$

where the enthalpy of species k is

$$h_k(\bar{T}) = h_k^0(T_{ref}) + \int_{T_{ref}}^{\bar{T}} c_{p,k}(T)dT. \tag{2.8}$$

The Favre averaged species mass fractions $\widetilde{Y}_k$ in Eq. (2.7) and the source term of the progress variable $\bar{\dot{\omega}}_C$ in Eq. (2.5) are interpolated from a pre-computed chemistry table. The table is parametrized by $\widetilde{Z}$, $\widetilde{Z''^2}$, and $\widetilde{C}$, where a presumed β-PDF with mean $\widetilde{Z}$ and variance $\widetilde{Z''^2}$ and a δ-PDF are used for the mixture fraction and for the progress variable, respectively, and statistical independence between mixture fraction and the reaction progress parameter is assumed. The species mass fractions and the progress variable source term can then be written as

$$\widetilde{Y}_k = \widetilde{Y}_k(\widetilde{Z}, \widetilde{Z''^2}, \widetilde{C}), \tag{2.9}$$

$$\bar{\dot{\omega}}_C = \bar{\dot{\omega}}_C(\widetilde{Z}, \widetilde{Z''^2}, \widetilde{C}). \tag{2.10}$$

After the temperature $\bar{T}$ has been computed from Eq. (2.7) with a Newton iteration, the equation of state for an ideal gas is used to close the system:

$$\bar{p} = \bar{\rho} R \bar{T} \sum_{k=1}^{k=N} \frac{\widetilde{Y}_k}{W_k}, \tag{2.11}$$

where R is the universal gas constant and W_k the molecular weight of species k.

Finally, the different mixture properties, i.e., viscosity μ, heat conduction coefficient λ, heat capacity c_p, and scalar diffusion coefficient $\bar{\rho}D$ are computed from mixing rules and properties of the different species as a function of temperature $\widetilde{T}$ and species mass fractions $\widetilde{Y}_k$ (Bird, Stewart & Lightfoot 2007).

2.2. *Numerical implementation*

The flow solver is a parallel solver for the solution of the compressible Navier-Stokes equations on unstructured meshes based on a finite volume formulation and implicit time-integration on arbitrary polyhedral mesh elements (Pecnik *et al.* 2008). The code is entirely written in C++ and uses subdomain decomposition and MPI as the parallel

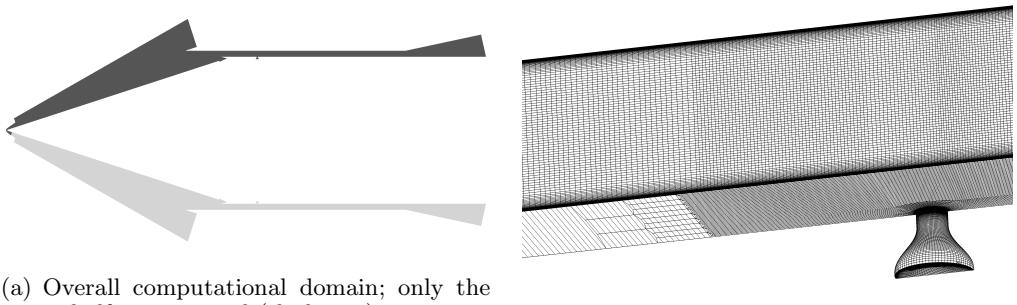

(a) Overall computational domain; only the upper half is computed (*dark grey*).

(b) Detail of the transition from two-dimensional to three-dimensional mesh and of the injector mesh.

FIGURE 1. HyShot II geometry.

infrastructure. The states at the cell faces are reconstructed with a second-order interpolation in conjunction with slope limiters, and the convective fluxes are computed with the HLLC approximate Riemann solver (Batten, Leschziner & Goldberg 1997). In this study a modified version of the Barth-Jespersen smooth limiter (Barth & Jespersen 1989) is used. The steady scalar equations are solved at each time step. Different turbulence models are implemented, e.g., Spalart-Allmaras, Wilcox k-ω, k-ϵ, k-ω SST. Only results based on the Spalart-Allmaras are shown here.

3. Simulation of the HyShot II ground experiment

The ground-based experiment in the High Enthalpy Shock Tunnel (HEG) at the German Aerospace Center (DLR) of a 1:1 model of the HyShot II vehicle (Gardner *et al.* 2004; Karl *et al.* 2008) is investigated in this study. This ground-based experiment provides a more exhaustive data set than the original HyShot II scramjet flight experiment, which was devised by The University of Queensland to achieve supersonic combustion in flight above Mach 7.5 using a simple ballistic reentry vehicle (Smart, Hass & Paull 2006).

3.1. *Flow configuration*

The overall HyShot II geometry and the computational domain are shown in Fig. 1(a), where only the upper half of the vehicle is considered. The HyShot II vehicle consists of a wedge intake and a combustor with constant area terminated by an exhaust nozzle. A bleed channel is located just before the entrance of the combustor to swallow the shock induced by the leading edge of the combustor top wall and the intake ramp boundary layer. Hydrogen is injected shortly after the combustion chamber entrance and auto-ignites downstream after sufficient mixing. The length of the constant area section of the combustor is approximately 300 mm, the height is 9.8 mm. The width of the combustor is 75 mm with four equally spaced porthole injectors located 58 mm after the combustion chamber entrance.

The overall computational mesh contains 5.4 millons cells. Only one eighth of the combustor span is simulated to reduce the computational cost. The mesh perpendicular to the walls is clustered near the wall to ensure enough resolution at the wall ($y^+ < 1$). Because the flow around the wedge intake is mostly two-dimensional and becomes only three-dimensional at the injection, the mesh was created with only 1 cell in the spanwise

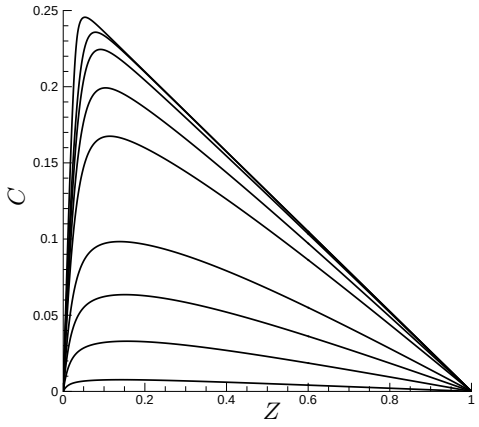

FIGURE 2. Progress variable C as a function of the mixture fraction Z for different flamelets parametrized by the stoichiometric scalar dissipation rate χ_{st} ranging from 0.002 to 1080.

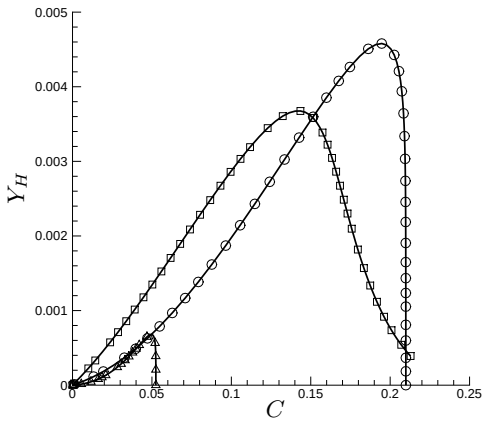

FIGURE 3. Mass fraction of species H as a function of the progress variable C for $Z = Z_{st} = 0.028$ (*squares*), $Z = 0.2$ (*circles*) and $Z = 0.8$ (*triangles*).

direction until about 10 injection nozzle diameters upstream of the injection nozzle. In a transition region between ten and seven diameters upstream of the injector, the mesh is gradually refine to a fully three-dimensional mesh. Details of the transition can be seen in Fig. 1(b). Symmetry boundary conditions are used at the spanwise boundary planes located in the center of one of the porthole injectors ($z = 0$ mm) and between this injector and the next one ($z = 9.375$ mm). No-slip boundary conditions are used at the walls and extrapolation of the conservative variables is applied at the exhaust.

The free stream inflow conditions chosen correspond to a flight Mach number $M_f = 7.4$ with a static pressure $P = 1813$ Pa, temperature $T = 242$ K, flow velocity $U = 2313$ m/s, and Reynolds number $Re \approx 3.8 \cdot 10^6$ m^{-1} (Karl *et al.* 2008). An isothermal wall boundary condition with $T_w = 300$ K is used since wall heating can be neglected owing to the very short duration of the experiment. Finally, the fuel inlet is prescribed to be at a total pressure of $p_t = 4.6$ bar and a temperature of $T = 300$ K to achieve an equivalence ratio $\phi \approx 0.3$.

3.2. *Chemistry model*

The chemistry model is based on the GRI-Mech v3.0 mechanism modified with new OH thermodynamics data (Herbon *et al.* 2002) and new H+O_2+M rates (Bates *et al.* 2001). The nine species considered are nitrogen (N_2), molecular and atomic oxygen and hydrogen (O_2, O, H_2, H), water (H_2O), hydrogen peroxide (H_2O_2), and the hydroxyl and hydroperoxyl radicals (OH, HO_2). The mechanism consists of 28 reactions. Nitrogen chemistry is not considered in this model.

The chemistry table has been created from a series of flamelet computations using the Flame-Master code. The pressure was chosen to correspond to an approximate average combustor pressure of $P = 1.5$ bar, whereas the boundary conditions were set to $T_O = 1300$ K for the oxidizer and $T_F = 300$ K for the fuel. The progress variable is defined as the mass fraction of water, i.e., $C = Y_{H_2O}$.

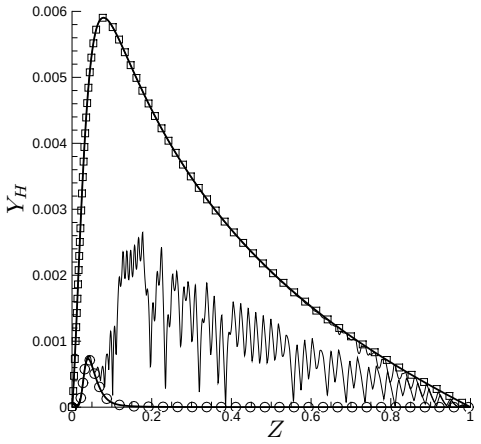

(a) Mass fraction of H as a function of the mixture fraction Z.

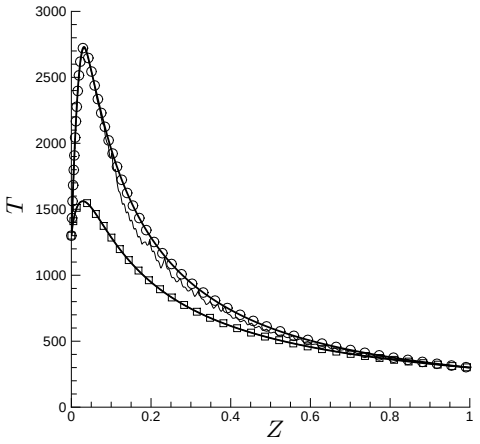

(b) Temperature T in K as a function of the mixture fraction Z.

FIGURE 4. Comparison of the interpolation on a structured Cartesian mesh (*thin line*) and on the new structured curvilinear mesh (*thick line*) with the exact solution for two different stoichiometric scalar dissipation rates $\chi_{st} = 0.014$ (*circles*) and $\chi_{st} = 653$ (*squares*).

3.3. *Chemistry tabulation*

As mentioned in section 2.1 the species mass fractions are computed in a preprocessing step and tabulated as a function of the mean $\widetilde{Z}$ and variance $\widetilde{Z''^2}$ of the mixture fraction and of the progress variable $\widetilde{C}$. The preprocessing step consists in solving one-dimensional diffusion flamelets parametrized by the scalar dissipation rate χ. In a second step those solutions are convoluted with a β-PDF and tabulated along the three dimensions $\widetilde{Z}$, $\widetilde{Z''^2}$, and $\widetilde{C}$. The classical tabulation approach is to interpolate the different flamelet solutions onto a structured Cartesian mesh spanning the complete range of the three variables $\widetilde{Z}$, $\widetilde{Z''^2}$, and $\widetilde{C}$. However, in the present case such a tabulation is not optimal because a large part of the domain, i.e., at large C values around $Z = 0$ and $Z = 1$, does not contain much information as shown in Fig. 2. Moreover, all the flamelets converge toward a similar C value when Z tends to 0 or 1. Therefore, a Cartesian mesh cannot differentiate between flamelet solutions in those regions. This is also illustrated in Fig. 3 where one can see that the mass fraction of species H varies dramatically for very small variations of C. To circumvent this issue, a different tabulation approach has been developed where the flamelets themselves are used in the progress variable direction as a grid, i.e., information is stored along flamelet solutions. Although this new tabulation is still structured, it is no longer Cartesian but curvilinear and the coordinate vector along the C direction becomes a function of Z. This has the great advantage of offering a good resolution at large and small values of Z, of avoiding unnecessary data storage where it is not needed, and of avoiding a interpolation step from the flamelet solutions to the mesh.

The lookup algorithm is still very similar to a Cartesian tabulation. Assuming a trilinear interpolation and given a Z and C value, one has first to find the two mixture fraction values Z_i and Z_{i+1} bounding the lookup coordinate Z. Then the four points $C_{i,j}$, $C_{i,j+1}$, $C_{i+1,j}$, and $C_{i+1,j+1}$ surrounding the lookup coordinate C must be determined. The final step is simply a trilinear interpolation of the variable of interest between these four points. The extension to a third dimension, e.g., $\widetilde{Z''^2}$, follows the same algorithm.

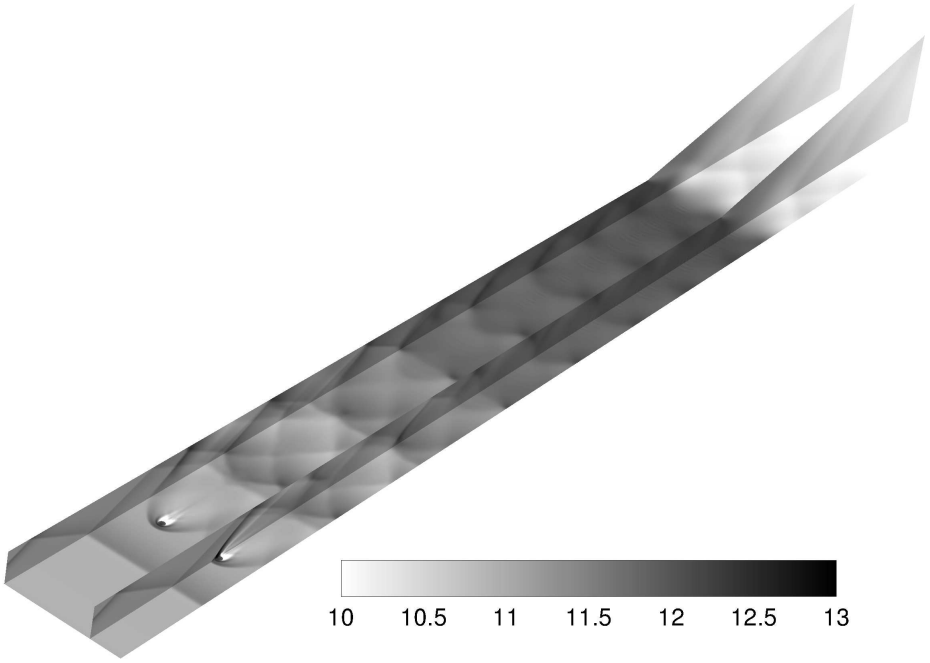

(a) Log of pressure $\bar{P}$.

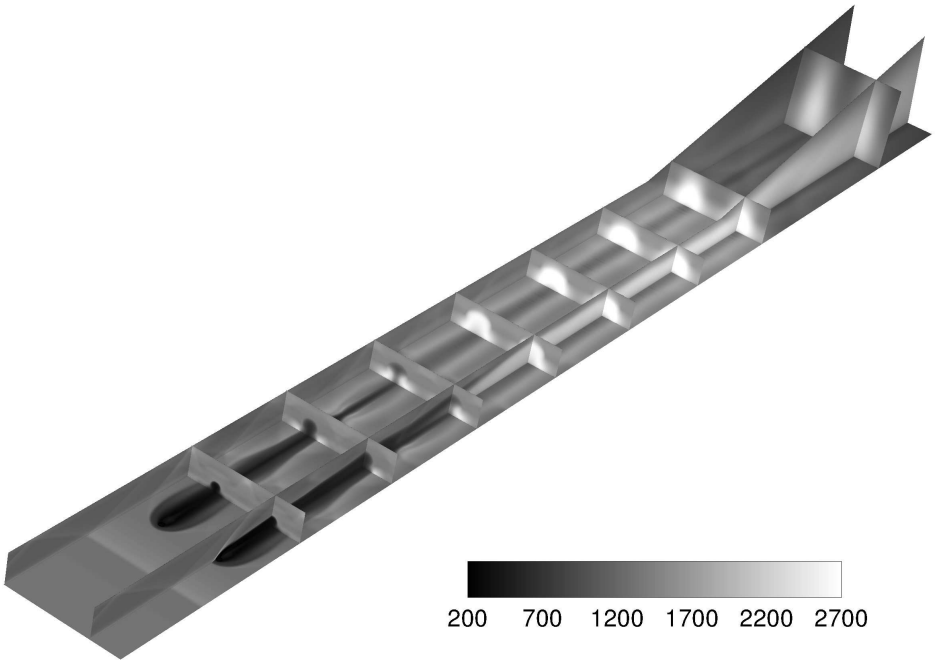

(b) Temperature $\bar{T}$ in K.

FIGURE 5. Contour visualization of the temperature and pressure along two symmetry planes going through and between two injectors, along the bottom wall and at different cross-planes.

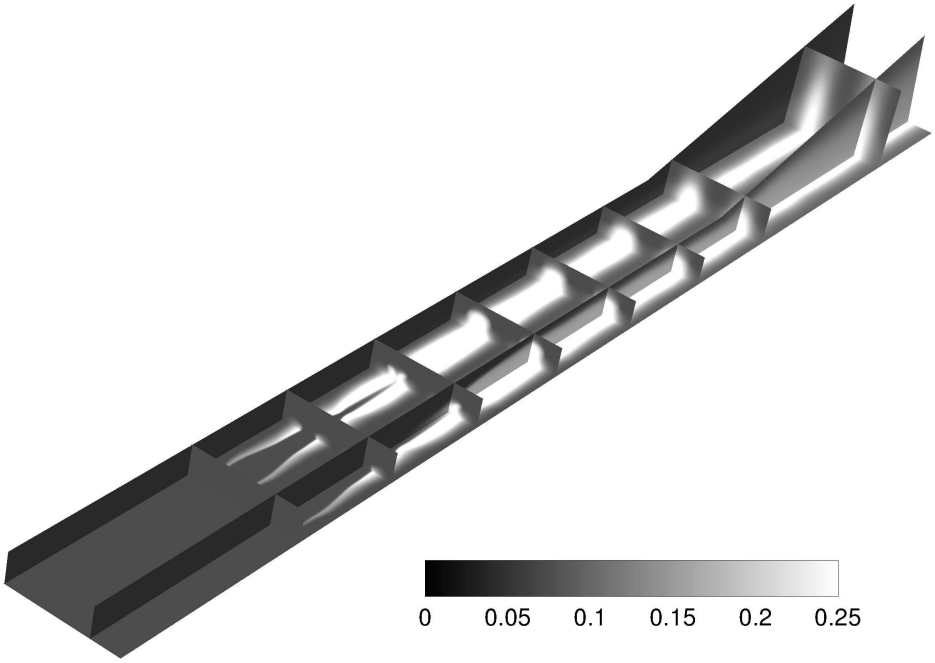

(a) Water mass fraction $\widetilde{Y}_{H_2O}$.

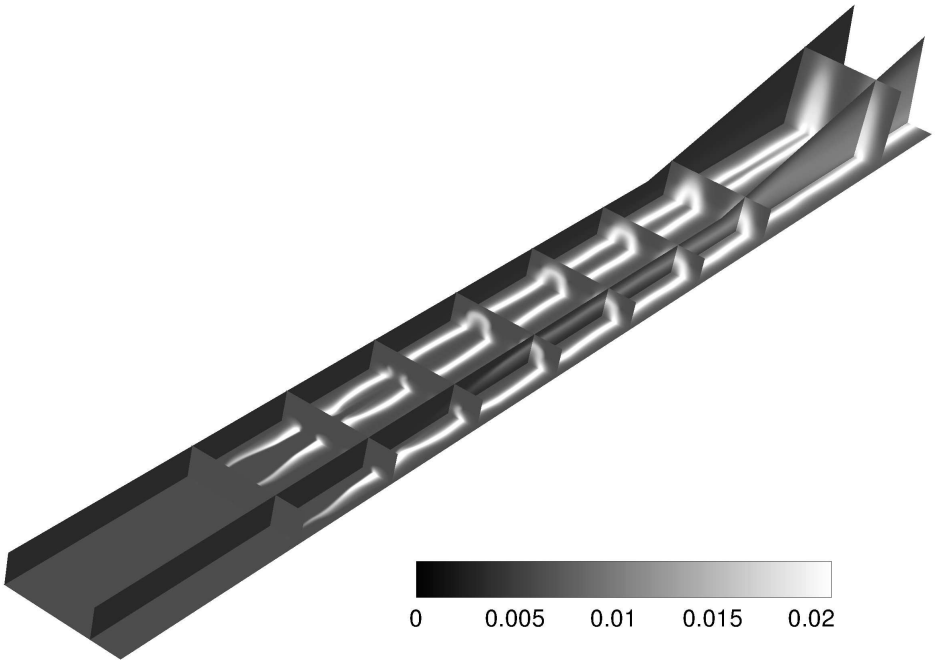

(b) OH mass fraction $\widetilde{Y}_{OH}$.

FIGURE 6. Contour visualization of the mass fraction of H_2O and OH along two symmetry planes going through and between two injectors, along the bottom wall and at different cross-planes.

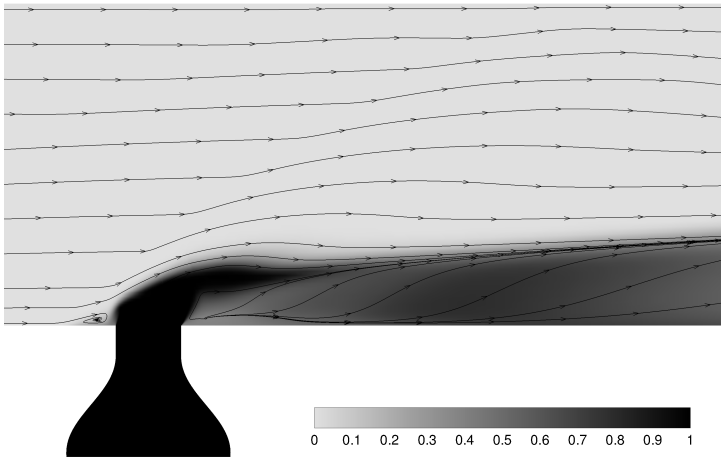

FIGURE 7. Contour visualization of the mixture fraction $\widetilde{Z}$and streamlines (black) in the symmetry plane going through the injector.

The classical structured Cartesian and the new structured curvilinear tabulations are compared in Fig. 4. One can see on Fig. 4(a) that the Cartesian interpolation leads to dramatic spurious oscillations for the species mass fraction especially at small stoichiometric scalar dissipation rate χ_{st}. On the other hand, the new curvilinear tabulation shows a very smooth interpolation without any oscillation. The same result is seen in the computation of the temperature as illustrated in Fig. 4(b). This demonstrates that the small additional lookup cost in a curvilinear mesh is largely compensated by a much smoother interpolation. Other alternatives exist to avoid those unwanted lookup oscillations, like Artificial Neural Networks (ANN) (Ihme, Marsden & Pitsch 2008) or unstructured tables (Shunn 2009), but the simplicity and accuracy of this approach makes it very attractive in this particular case.

4. Results

Figures 5 and 6 show contours of pressure, temperature, and mass fraction of H_2O and OH along the combustor. A two-dimensional shock train emanates from the leading edge of the combustor bottom wall reflecting on the top and bottom walls as shown in Fig. 5(a). In addition a bow shock is formed upstream of the fuel jet and interacts in a complex three-dimensional shock system with the shock train. Unlike the unfueled combustor, this complex shock system is highly three-dimensional. One can also observe in Figs. 5(b) and 6(a) that the the flame is not anchored at the injector but at a downstream distance of approximately 9 cm, owing to the effect of finite rate chemistry. In the boundary layer, ignition takes place earlier, i.e., approximately 4 cm after injection, due to lower velocities and thus, longer residence time. A maximum average temperature of 2600 K is reached at the end of the combuster, shortly before the nozzle. Around 80% of the fuel is burned within the combustor, an additional 10% is burned in the exhaust nozzle. Figure 6(b) indicates that a non-negligible amount of OH is still present at the exhaust. The OH contour clearly shows that the flame is located around the hydrogen flow.

Streamlines in the plane of symmetry through the injector are shown in Fig. 7. The penetration of the fuel jet is around 20% of the combustion chamber height. Two counter-

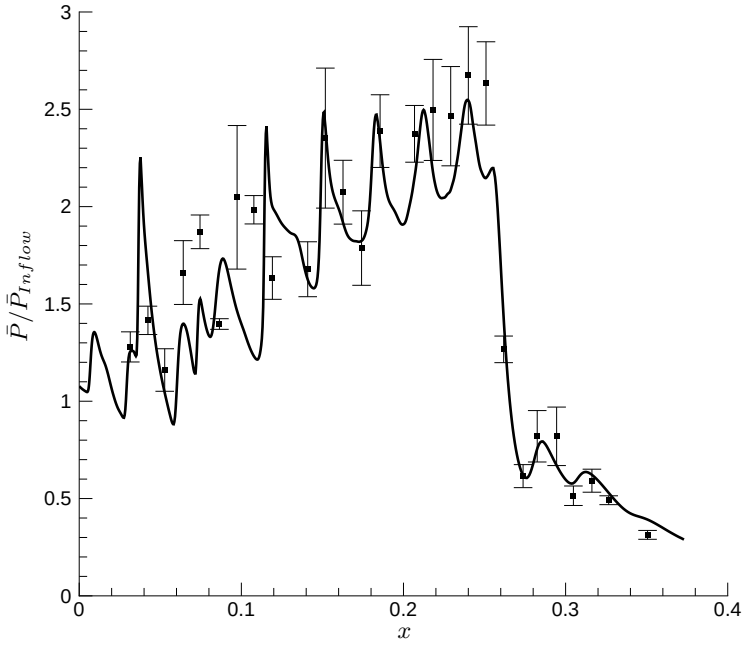

FIGURE 8. Pressure distribution in the combustion chamber along the bottom wall between two hydrogen injectors. The pressure is normalized by the combustor inflow pressure. The injector is located at $x = 0$ and the symbols correspond to the measurements of the DLR ground experiment.

rotating recirculation bubbles are located in front of the jet strongly enhancing the diffusion of the fuel in the boundary layer of the bottom combustor wall. Behind the injector a complicated vortex system is formed, also contributing to the fuel mixing.

The pressure along the centerline of the combustor, i.e., between two injectors, is depicted in Fig. 8. The comparison with the experimental data of the DLR ground test shows relatively good agreement. The overall pressure level is slightly lower than the measurements. This could be the result of the neglected three-dimensional effects of the combustor side walls, in particular the shock train formed at the leading edge on the side walls, which has been shown to be non-negligible.

5. Conclusions and future work

The present results are very promising and demonstrate that a flamelet approach seems to be feasible to simulate high-speed flows, although many aspects are still to be evaluated.

The next steps will be to validate the combustion model with the jet in crossflow experiments performed at Stanford (Heltsley *et al.* 2007). The influence of the mixing, e.g., turbulent Schmidt number, and combustion model on flame location will be investigated. The statistical independence between the mixture fraction and the progress variable and the presumed δ-PDF for $\widetilde{C}$ will also be analyzed (Ihme, Cha & Pitsch 2005).

The flamelet model has been derived and extensively used for low Mach number flows. However, the low Mach number assumptions do not hold anymore at supersonic speed where compressibility effects and viscous heating play a major role. Although these effects

are considered in the above formulation by computing the temperature from the species mass fractions and the energy, the species mass fractions themselves are only functions of the mixture fraction Z and the progress variable C. In other words, compressibility effects and viscous heating are not considered in the computation of the chemistry table. Future work will attempt to quantify the sensitivity of the species mass fractions, and thus, of the computed temperature, on compressibility effects and viscous heating. Depending on the criticality of these effects, the combustion model could be improved by adding one or more dimensions to the chemistry table, e.g., pressure, energy.

A parallel effort will focus on improving the flow solver to achieve more robustness and increase the computational speed. Different options will be tested like pre-tabulation of the temperature and mixture properties, dual-time stepping and/or coupling scalar and Navier-Stokes solve.

Finally, the unstart phenomenon will be investigated in the HyShot II geometry by increasing the fuel flow rate. The goal is to identify the critical parameters controlling the unstart and understand its dynamics.

Acknowledgments

This work was supported by the United States Department of Energy under the Predictive Science Academic Alliance Program (PSAAP) at Stanford University.

REFERENCES

Barth, T. J. & Jespersen, D. 1989 The design and application of upwind schemes on unstructured meshes. *AIAA Paper 89-0366*.

Bates, R. W., Golden, D. M., Hanson, R. K. & Bowman, C. T. 2001 Experimental study and modeling of the reaction $H+O_2+M \rightarrow HO_2 + M$ (M=Ar, N_2, H_2O) at elevated pressures and temperatures between 1050 and 1250 K. *Phys. Chem. Chem. Phys.* **3**(12), 2337–2342.

Batten, P., Leschziner, M. A. & Goldberg, U. C. 1997 Average-state Jacobians and implicit methods for compressible viscous and turbulent flows. *J. Comput. Phys.* **137**(1), 38–78.

Baurle, R., Hsu, A. & Hassan, H. 1995 Assumed and Evolution Probability Density Functions in Supersonic Turbulent Combustion Calculations. *J. of Propulsion and Power* **11**(6), 1132–1138.

Baurle, R. & Girimaji, S. 2003 Assumed PDF turbulence-chemistry closure with temperature-composition correlations. *Combustion and Flame* **134**, 131–148.

Berglund, M. & Fureby, C. 2007 LES of supersonic combustion in a scramjet engine model. *Proceedings of the Combustion Institute* **31**, 2497–2504.

Birbaud, A.L. & Pitsch, H. 2008 Combustion noise modeling using compressible simulations. *Annual Research Briefs 2008.* Center for Turbulence Research, Stanford University/NASA Ames, 339–346.

Bird, R.B., Stewart, W.E. & Lightfoot, E.N. 2007 *Transport Phenomena*, John Wiley & Sons, Inc.

Bray, K.N.C. 1996 The challenge of turbulent combustion. *Proceedings of the Combustion Institue*, 1–26.

Chakraborty, D., Paul, P. & Mukunda, H. 2000 Evaluation of combustion models

for high speed H2/air confined mixing layer using DNS data. *Combustion and Flame* **121**, 195–209.

Cook, D. J., Pitsch, H., Chen, J. H. & Hawkes, E. R. 2007 Flamelet-based modeling of auto-ignition with thermal inhomogeneities for application to HCCI engines. *Proceedings of the Combustion Institute* **31**, 2903–2911.

Davidenko, D., Gokalp, I., Dufour, E. & Magre, P. 2003 Numerical simulation of hydrogen supersonic combustion and validation of computational approach. *AIAA Paper 2003-7033*.

Gardner, A. D., Hannemann, K., Steelant, J. & Paull, A. 2004 Ground Testing of the HyShot Supersonic Combustion Flight Experiment in HEG and Comparison with Flight Data. *AIAA Paper 2004-3345*.

Genin, F., Chernyavsky, B. & Menon, S. 2004 Large Eddy Simulation of Scramjet Combustion Using a Subgrid Mixing/Combustion Model. *AIAA Paper 2004-7035*.

Heltsley, W. N., Snyder, J. A., Cheung, C. C., Mungal, M. G. & Hanson, R. K. 2007 Combustion Stability Regimes of Hydrogen Jets in Supersonic Crossflow. *AIAA Paper 2007-5401*.

Herbon, J. T., Hanson, R. K., Golden, D. M. & Bowman C. T. 2002 A Shock Tube Study of the Enthalpy of Formation of OH. *Proceedings of the Combustion Institute* **29**, 1201–1208.

Ihme, M., Cha, C. M. & Pitsch, H. 2005 Prediction of local extinction and re-ignition effects in non-premixed turbulent combustion using a flamelet/progress variable approach. *Proceedings of the Combustion Institute* **30**, 793–800.

Ihme, M., Marsden, A. L. & Pitsch, H. 2008 Generation of Optimal Artificial Neural Networks Using a Pattern Search Algorithm: Applications to Approximation of Chemical Systems. *Neural Computation* **20**, 573–601.

Karl, S., Hannemann, K., Mack, A. & Steelant, J. 2008 CFD Analysis of the HyShot II Scramjet Experiments in the HEG Shock Tunnel. *AIAA Paper 2008-2548*.

Pecnik, R., Constantine, P., Ham, F. & Iaccarino, G. 2008 A probabilistic framework for high-speed flow simulations. *Annual Research Briefs 2008.* Center for Turbulence Research, Stanford University/NASA Ames, 3–17.

Peters, N. 2000 *Turbulent Combustion*, Cambridge University Press.

Pierce, C. D. & Moin, P. 2004 Progress-variable approach for large-eddy simulation of non-premixed turbulent combustion. *J. Fluid Mech.* **504**, 73–97.

Pitsch, H. 2006 Large-Eddy Simulation of Turbulent Combustion. *Annu. Rev. Fluid Mech.* **38**, 453–382.

Poinsot, T. & Veynante, D. 2005 *Theoretical and Numerical Combustion*, R. T. Edwards, Inc., Philadelphia, PA.

Shunn, L. 2009 *Large-Eddy-Simulation of combustion systems with convective heat loss.* Ph.D. thesis, Stanford University, California.

Smart, M. K., Hass, N. E. & Paull, A. 2006 Flight Data Analysis of the HyShot 2 Scramjet Flight Experiment. *AIAA Journal* **44**(10), 2366–2375.

Sunami, T., Magre, P., Bresson, A., Grisch, F., Orain, M. & Kodera, M. 2005 Experimental Study of Strut Injectors in a Supersonic Combustor Using OH-PLIF. *AIAA Paper 2005-3304*.

Waidmann, W., Alff, F., Boehm, M., Brummund, U., Clauss, W. & Oschwald, M. 1996 Supersonic Combustion of Hydrogen/Air in a Scramjet Combustion Chamber. *Space Technology* **15**(6), 421–429.